Soft Matter

Non-isothermal cold crystallization of liquid crystalline porphyrins

Journal:	*Soft Matter*
Manuscript ID	SM-ART-06-2023-000760.R1
Article Type:	Paper
Date Submitted by the Author:	28-Jul-2023
Complete List of Authors:	Dorfner, Alec; Siena College, Chemistry and Biochemistry Locoteta, Diana; Siena College, Chemistry and Biochemistry Messinger, Caleb; Siena College, Chemistry and Biochemistry Ramsey, Michael; Siena College, Chemistry and Biochemistry Kim, Nathaniel; Siena College, Chemistry and Biochemistry Sadzaglishvili, Elene; Siena College, Chemistry and Biochemistry Kranick, Joshua; Siena College, Chemistry and Biochemistry Kuehner, Joseph; Siena College, Chemistry and Biochemistry Timony, Collin; Siena College, Chemistry and Biochemistry Langton, Michelle; Siena College, Chemistry and Biochemistry Winklarek, Jeffrey; Siena College, Chemistry and Biochemistry Tucker, Lucas; Siena College, Chemistry and Biochemistry O'Donnell, Jodi; Siena College, Chemistry and Biochemistry

ARTICLE

Non-isothermal cold crystallization of liquid crystalline porphyrins

Alec L. Dorfner, Diana P. Locoteta, Caleb D. Messinger, Michael R. Ramsey, Nathaniel Y. Kim, Elene Sadzaglishvili, Joshua C. Kranick, Joseph S. Kuehner, Collin J. Timony, Michelle Langton, Jeffrey E. Winklarek, Lucas J. Tucker, Jodi L. O'Donnell*

Received 00th January 20xx,
Accepted 00th January 20xx

DOI: 10.1039/x0xx00000x

A series of liquid crystalline porphyrins was synthesized, purified, and characterized. Differential scanning calorimetry (DSC) and hot-stage polarized optical microscopy (HS-POM) revealed that the porphyrins in the series with shorter alkyl arm lengths exhibit kinetic cold crystallization, wherein the molecules spontaneously organize into large, disc-like structures that remain stable upon cooling. Using DSC, the kinetic and thermodynamic parameters related to these materials were determined. Analysis of non-isothermal crystallization revealed the presence of multiple nucleation and growth processes related to cold crystallization.

Introduction

Porphyrins have been extensively studied for applications including use in optoelectronic devices,[1] molecular photovoltaics,[2] chemical sensors,[3] and other materials that benefit from rich coloration, π-delocalized structure, and chemical tailorability achieved through the addition of metals and other synthetic modifications.[4] In many potential applications of porphyrinic materials, control of molecular orientation and stacking is crucial for functional device fabrication.

Porphyrins are well-suited for generating columnar discotic liquid crystals due to their rigid aromatic core, which can easily be substituted with flexible arms.[5–7] Liquid crystalline behavior, including partial long-range order, is commonly observed for molecules with a π-conjugated rigid core and flexible side chains,[8–10] including those possessing a porphyrin core.[5–7,11] The disorder introduced by the flexible side chains leads to soft and mobile materials.[12] While cold crystallization is primarily reported for polymeric species, an increasing number of studies detail cold crystallization in small molecules, particularly those that are soft, mobile, and approximately C_2 symmetric.[8-10,12-17]

Differential scanning calorimetry (DSC) analysis of liquid crystals has revealed that cooling from an isotropic liquid can sometimes lead to the formation of a supercooled amorphous solid without crystallization.[17] When this amorphous solid is heated again, an exothermic cold crystallization event may occur following the glass transition.[18] Achieving long-range order by aligning the rigid cores and packing the side chains is a slow process. Consequently, crystal formation during rapid cooling from the liquid can be hindered by the limited mobility of the side chains. The subsequent heating cycle increases molecular mobility, triggering an increase in crystalline order for which an exotherm is observed while heat is being added to the material.[12] This crystal growth can be further observed using hot-stage polarized optical microscopy (HS-POM).

Herein, we describe the synthesis and characterization of four liquid crystalline porphyrins with varying alkyl arm lengths, Scheme 1. In addition to flexible arms, we introduced a domain of relative rigidity to the termini of the arms. Our goal was to produce helical columnar discotic liquid crystals to induce long range order and its associated optoelectronic properties. We investigate the liquid crystalline properties and crystallization kinetics of all four species using non-isothermal DSC and HS-POM. For the two species that exhibit a cold crystallization event, we provide a detailed analysis of their crystallization kinetics.

Experimental

Materials and general methods

All reagents were purchased from commercial sources and used as received.

^{1}H and ^{13}C nuclear magnetic resonance (NMR) spectra for all products were recorded on a Bruker 500 MHz Avance HD NMR Spectrometer in $CDCl_3$ at 500 and 125 MHz, respectively; chemical shifts were determined with respect to $CHCl_3$ residual signals. Matrix-assisted laser desorption and ionization time-of-flight mass spectrometry (MALDI-TOF MS) was performed on a Bruker Autoflex Speed MALDI Mass Spectrometer using saturated α-cyano-4-hydroxycinnamic acid (HCCA) in acetone as the matrix. Thermogravimetric analysis (TGA) was performed on a TA Instruments Q500 Thermogravimetric Analyzer using ceramic pans and High-Res Dynamic mode. Samples were heated from 25 °C to 900 °C with a heating rate of 50 °C/min.

Optical textures were investigated using an Olympus BX51 Polarizing Optical Microscope and an Instec STC200 heated

Siena College, Department of Chemistry and Biochemistry, 515 Loudon Road, Loudonville NY, 12211, USA

Electronic Supplementary Information (ESI) available: ^{1}H and ^{13}C NMR, MALDI-TOF MS, TGA, MDSC, and HS-POM. See DOI: 10.1039/x0xx00000x

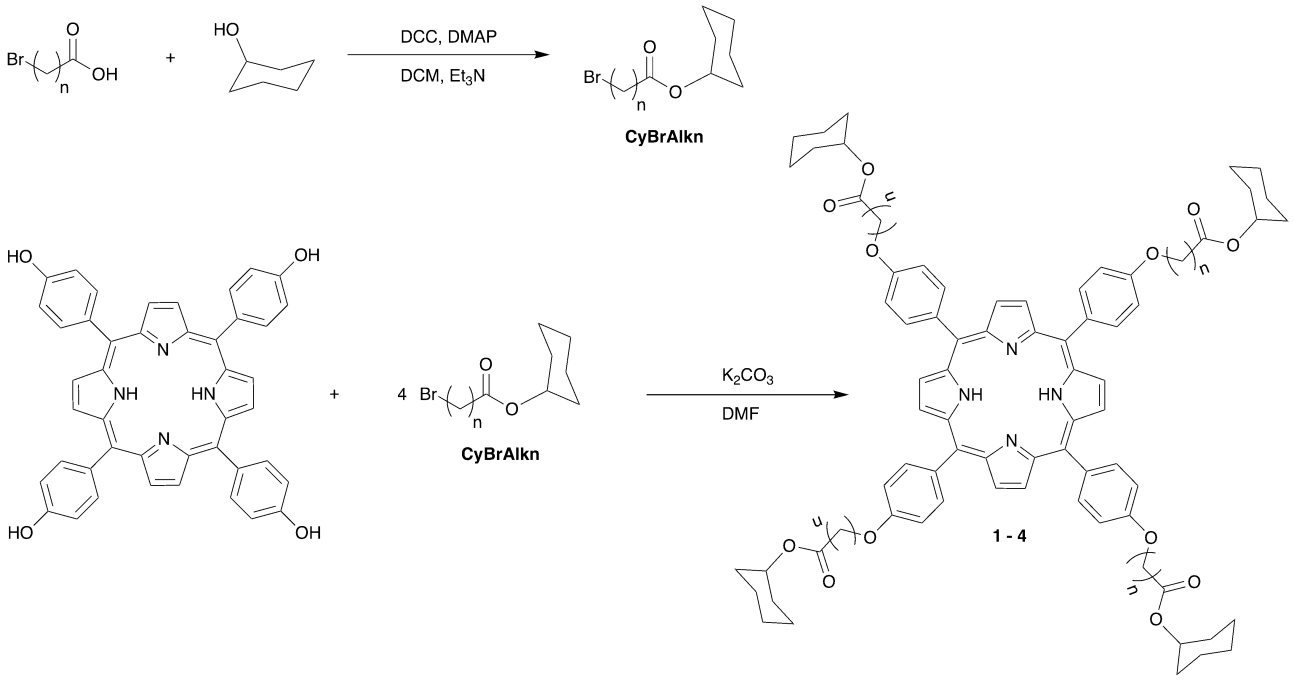

Scheme 1 Synthesis of **1 – 4**.

stage (heat rate 100 °C/min) and photographed with an Olympus DP20 microscope camera. Samples for texture analysis were prepared by dissolving compounds in minimal solvent (5:4 volumetric ratio of acetone:chloroform) and pipetting the solution onto a glass microscope slide that had been rubbed unidirectionally 50 times with a Kimwipe. Film thicknesses were measured by cross-sectional SEM analysis using a Hitachi SU1510 Scanning Electron Microscope.

All calorimetry data were collected on a TA Instruments Q2000 Differential Scanning Calorimeter. Two to three milligrams of each compound were loaded into Tzero pans and sealed with hermetic lids. Non-isothermal data were collected using repeated heat-cool-heat cycles in the dynamic range of –40 °C to 240 °C with heating rates of 2, 5, 10, 20, 30, 40, and 50 °C/min. Modulated DCS (MDSC) traces were collected in the same dynamic range as non-isothermal DSC with modulation rate of 3 °C/min, amplitude of ± 1 °C, and period of 60 s.

Synthetic procedures

Preparation of cyclohexyl n-bromoalkanoates (CyBrAlkn, n = 6, 8, 10, 12)[19,20] A pear-bottom flask was charged with N,N′-dicyclohexylcarbodiimide (DCC, 0.949 g, 4.6 mmol), DMAP (15 mg, cat.), and n-bromoalkanoic acid (n = 6, 0.897 g; n = 8, 1.026 g; n = 10, 1.155 g; n = 12 1.285 g, 4.6 mmol). Cyclohexanol (0.461 g, 4.6 mmol) was added and immediately followed by 3-6 drops of triethylamine. The reaction mixture was stirred by hand with a glass stir rod for 45 min. The crude reaction mixture was combined with 6 mL cold hexanes and filtered through a Celite plug to collect the eluate which was cooled to –20 °C for 18 hrs. Solids that precipitated upon cooling were removed via vacuum filtration and removal of hexanes in vacuo from the remaining eluate yielded pale yellow oils that were then stored at –20 °C.

cyclohexyl 6-bromohexanoate. 0.8343 g, 65.4% yield. ^{1}H NMR (500 MHz, $CDCl_3$) δ 4.69 (m, 1H, COO-C*H*), 3.34 (t, *J* = 6.8 Hz, 2H, Br-CH_2), 2.24 (t, *J* = 7.5 Hz, 2H, -CH_2-COO-), 1.85 – 1.15 (m, 16H, alkyl CH_2); ^{13}C NMR (125 MHz, $CDCl_3$) δ 172.82, 72.43, 34.44, 33.41, 32.41, 31.63, 27.61, 25.40, 24.19, 23.73.

cyclohexyl 8-bromooctanoate. 0.9373 g, 66.8% yield. ^{1}H NMR (500 MHz, $CDCl_3$) δ 4.69 (m, 1H COO-C*H*), 3.34 (t, *J* = 6.8 Hz, 2H, Br-CH_2), 2.22 (t, *J* = 7.5 Hz, 2H, -CH_2-COO-), 1.85 – 1.15 (m, 20H, alkyl CH_2); ^{13}C NMR (125 MHz, $CDCl_3$) δ 173.12, 72.29, 34.63, 33.76, 32.70, 31.65, 28.86, 28.38, 27.96, 25.42, 24.94, 23.74.

cyclohexyl 10-bromodecanoate. 1.2012 g, 78.3% yield. ^{1}H NMR (500 MHz, $CDCl_3$) δ 4.71 (m, 1H COO-C*H*), 3.35 (t, *J* = 6.8 Hz, 2H, Br-CH_2), 2.22 (t, *J* = 7.5 Hz, 2H, -CH_2-COO-), 1.85 – 1.16 (m, 24H, alkyl CH_2); ^{13}C NMR (125 MHz, $CDCl_3$) δ 173.22, 72.25, 34.72, 33.85, 32.81, 31.66, 29.23, 29.13, 29.04, 28.68, 28.13, 25.43, 25.06, 23.75.

cyclohexyl 12-bromododecanoate. 1.2665 g, 76.1% yield. ^{1}H NMR (500 MHz, $CDCl_3$) δ 4.71 (m, 1H COO-C*H*), 3.35 (t, *J* = 6.9 Hz, 2H, Br-CH_2), 2.22 (t, *J* = 7.5 Hz, 2H, -CH_2-COO-), 1.85 – 1.17 (m, 28H, alkyl CH_2); ^{13}C NMR (125 MHz, $CDCl_3$) δ 173.25, 72.23, 34.75, 33.88, 32.84, 31.67, 29.44, 29.39, 29.23, 29.10, 28.75, 28.17, 25.45, 25.09, 23.76.

Preparation of meso-tetrakis(4-CyAlknoxyphenyl)porphyrins[21] Meso-tetrakis(4-hydroxyphenyl)porphyrin (0.1000 g, 0.147 mmol) and cyclohexyl n-bromoalkanoate (**CyBrAlkn**) (n = 6, 0.4901 g; n = 8, 0.5397 g; n = 10, 0.5893 g; n = 12, 0.6389 g, 1.77 mmol) were dissolved in 0.250 mL dimethylformamide (DMF). Potassium carbonate (0.1628 g, 1.18 mmol) was added, and the mixture was stirred at 80 °C. After 24 hours, an additional 0.250 to 0.500 mL DMF was added to each reaction mixture to dissolve solids deposited on the flask wall. After 48 hours, the

reaction mixture was cooled to room temperature and combined with 30 mL ethyl acetate. It was then filtered through Celite, washed with 1 M $NaHSO_4$ (3 x 25 mL), saturated brine (1 x 25 mL), dried over $MgSO_4$, and filtered. The solvent was removed via rotary evaporation. The product was further purified by preadsorbing the crude product onto silica, loading it onto a silica gel plug, rinsing with 100 mL hexanes, 125 mL methanol, and then flushing off the main purple product with chloroform. The chloroform volume was reduced to ca. 1 mL via rotary evaporation and the concentrated solution was poured over 75 mL cold swirling hexanes. The suspension was transferred to centrifuge tubes and centrifuged at 4000 rpm for 5 minutes. The supernatant was decanted and the pellet was resuspended in hexanes, centrifuged for 5 additional minutes, and decanted again. The pellet was resuspended in minimal hexanes, transferred to a round bottom flask, and dried in vacuo to yield an oily purple solid.

1, n = 6. 0.2178 g, 69.6% yield. ^{1}H NMR (500 MHz, $CDCl_3$) δ 8.87 (s, 8H, pyrrole *H*), 8.11 (d, *J* = 8.5 Hz, 8H, *o*-aryl-*H*), 7.26 (d, *J* = 8.6 Hz, 8H, *m*-aryl-*H*), 4.83 (m, 4H, COO-C*H*), 4.25 (t, *J* = 6.3 Hz, 8H, Ar-O-CH_2), 2.43 (t, *J* = 7.5 Hz, 8H, -CH_2-COO-), 2.07 – 1.23 (m, 64H, alkyl CH_2), –2.74 (s, 2H, pyrrole-N*H*); ^{13}C NMR (125 MHz, $CDCl_3$) δ 173.31, 159.03, 135.74, 134.71, 119.93, 112.85, 72.65, 68.12, 34.91, 31.88, 31.83, 29.36, 25.99, 25.59, 25.54, 25.13, 25.08, 23.95. MALDI-TOF MS: $[M + H]^+$ calcd for $C_{92}H_{110}N_4O_{12,}$ 1463.819; observed, 1463.558.

2, n = 8. 0.0490 g, 21.0% yield. ^{1}H NMR (500 MHz, $CDCl_3$) δ 8.86 (s, 8H, pyrrole *H*), 8.11 (d, *J* = 8.5 Hz, 8H, *o*-aryl-*H*), 7.28 (d, *J* = 8.6 Hz, 8H, *m*-aryl-*H*), 4.80 (m, 4H, COO-C*H*), 4.25 (t, *J* = 6.5 Hz, 8H, Ar-O-CH_2), 2.35 (t, *J* = 7.5 Hz, 8H, -CH_2-COO-), 1.98 – 1.18 (m, 80H, alkyl CH_2), –2.74 (s, 2H, pyrrole-N*H*); ^{13}C NMR (125 MHz, $CDCl_3$) δ 173.47, 159.10, 135.74, 134.65, 119.94, 112.86, 72.52, 68.40, 34.94, 31.86, 29.60, 29.31, 29.27, 26.24, 25.58, 25.56, 25.25, 23.93. MALDI-TOF MS: $[M + H]^+$ calcd for $C_{100}H_{126}N_4O_{12,}$ 1575.945; observed, 1575.702.

3, n = 10. 0.1142 g, 46.0% yield. ^{1}H NMR (500 MHz, $CDCl_3$) δ 8.86 (s, 8H, pyrrole *H*), 8.11 (d, *J* = 8.5 Hz, 8H, *o*-aryl-*H*), 7.28 (d, *J* = 8.6 Hz, 8H, *m*-aryl-*H*), 4.78 (m, 4H, COO-C*H*), 4.25 (t, *J* = 6.5 Hz, 8H, Ar-O-CH_2), 2.32 (t, *J* = 7.6 Hz, 8H, -CH_2-COO-), 1.98 – 1.26 (m, 96H, alkyl CH_2), –2.74 (s, 2H, pyrrole-N*H*); ^{13}C NMR (125 MHz, $CDCl_3$) δ 173.52, 159.12, 135.74, 134.64, 119.95, 112.86, 72.47, 68.48, 34.96, 31.84, 29.68, 29.61, 29.42, 29.31, 26.37, 25.58, 25.30, 23.92, 22.79. MALDI-TOF MS: $[M + H]^+$ calcd for $C_{108}H_{142}N_4O_{12,}$ 1688.070; observed, 1687.760.

4, n = 12. 0.1351 g, 50.6% yield. ^{1}H NMR (500 MHz, $CDCl_3$) δ 8.86 (s, 8H, pyrrole *H*), 8.11 (d, *J* = 8.5 Hz, 8H, *o*-aryl-*H*), 7.27 (d, *J* = 8.7 Hz, 8H, *m*-aryl-*H*), 4.77 (m, 4H) , COO-C*H*, 4.25 (t, *J* = 6.5 Hz, 8H, Ar-O-CH_2), 2.30 (t, *J* = 7.6 Hz, 8H, -CH_2-COO-), 1.98 – 1.27 (m, 112H, alkyl CH_2), –2.74 (s, 2H, pyrrole-N*H*); ^{13}C NMR (125 MHz, $CDCl_3$) δ 173.53, 159.13, 135.74, 134.63, 119.95, 112.86, 72.44, 68.51, 34.96, 31.83, 29.78, 29.73, 29.69, 29.65, 29.45, 29.30, 26.40, 25.58, 25.30, 23.91. MALDI-TOF MS: $[M + H]^+$ calcd for $C_{116}H_{158}N_4O_{12,}$ 1800.195; observed, 1799.809.

Results and discussion

Synthesis and characterization. Liquid crystalline porphyrins were synthesized, purified, and characterized by ^{1}H NMR, ^{13}C NMR, MALDI-TOF MS, and TGA. TGA analysis of all four species revealed similar thermal stabilities, with losses of cyclohexanol moieties at 338 °C and alkanoic acids at 410 °C. Non-isothermal DSC heat-cool-heat runs at 20 °C/min revealed glass transitions for **1** and **2** at 25 °C and 0 °C, respectively. No glass transitions were observed for **3** or **4**, as their glass transitions occur below the dynamic temperature range for the instrument (–40 to 240 °C).

When heated the second and subsequent times at variable rates, both **1** and **2** undergo kinetic cold crystallization, Fig. 1a and 1b, respectively. The activation energies were determined by the Kissinger equation to be 81 ± 10 kJ/mol for **1** and 108 ± 7 kJ/mol for **2**, suggesting that activation energy increases with alkyl chain length.[14,15] The entropies of cold crystallization for **1** and **2** are –100 J/mol·K and –112 J/mol·K, respectively, and entropies of fusion are 111 J/mol·K and 124 J/mol·K, respectively. These relatively large entropies are similar to those reported for other cold crystallizing liquid crystals and are indicative of a highly organized crystalline phase with limited molecular motion.[22,23] Kinetic cold crystallization was not observed for **3** and **4** as upon cooling they crystallize rather than form supercooled amorphous solids, Fig. 1c and 1d, respectively. It appears that **3** forms multiple mesophases upon fast cooling, which has been observed for other rod- and disc-like molecules.[23–25]

To further investigate the kinetic cold crystallization of **1** and **2**, MDSC data were collected in the same dynamic temperature range as non-isothermal DSC.[26] A phase diagram for **1** and **2** was constructed from the combined DSC and MDSC traces, Fig. 2. On heating, both **1** and **2** exhibit two distinct liquid crystalline phases**,** an isotropic transition that overlaps kinetic crystal perfection, and no apparent crystallization upon cooling. MDSC deconvoluted the thermal and kinetic events, revealing a second exothermic kinetic event, crystal perfection,[13] superimposed on the endothermic thermodynamic isotropic transition, indicated in Fig. 2 and in Fig. 1a and 1b as two apparent endotherms.

Texture investigation. Each species was deposited as a thin film (typically 0.3 to 1.0 microns) onto a glass slide and the phase changes observed in DSC were visualized with HS-POM. All four materials exhibit liquid crystalline textures. Very small (1 to 2 μm) oblong crystals appear when **1** is held between 25 and 75 °C. This growth is slow, with birefringence first observed after 60 minutes of heating at 60 °C, Fig. 3a. Between 75 and 130 °C, the formation of large disc-like crystals of **1** can be observed, Fig. 3b. The rate of crystal formation increases with increasing temperature. The small oblong crystals act as nucleation sites for the larger faster growing crystals. When **1** is heated to temperatures between 50 and 60 °C for over 120 minutes, fringes associated with the disc formation begin to become visible growing on the oblong crystals. Above 140 °C, the discs become fractured and disordered. Between 180 and

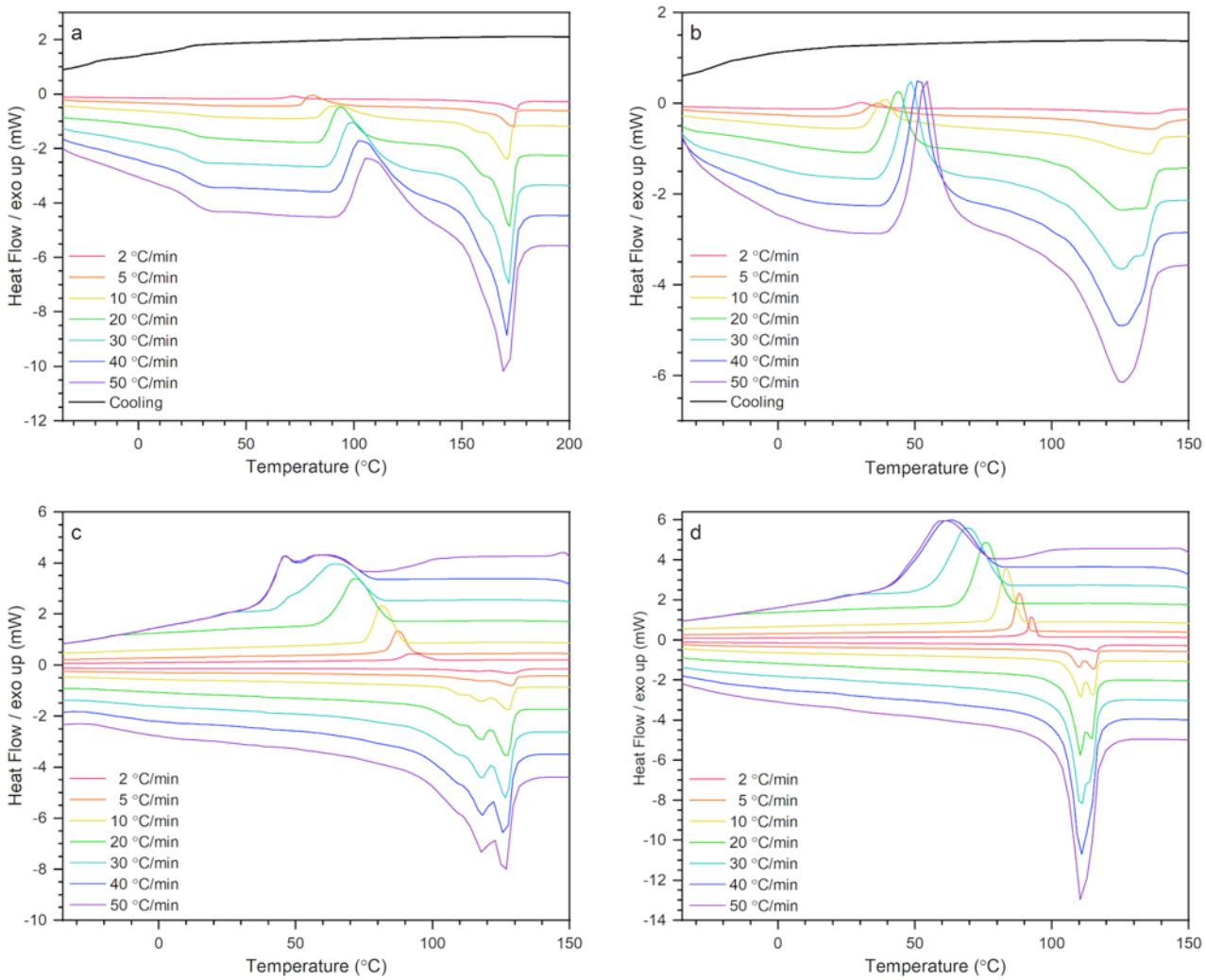

Fig. 1 Non-isothermal DSC for **1** – **4**, panels a – d, respectively.

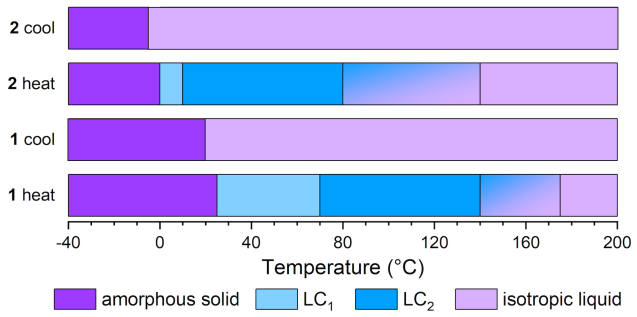

Fig. 2 Phases of **1** and **2** upon heating and cooling determined from MDSC.

190 °C, the crystalline order is completely obliterated, resulting in an isotropic liquid.

Heating a thin film of **2** from room temperature shows no crystallization. This is reasonable, as the glass transition temperature for **2** is 0 °C. When **2** is melted, cooled to –80 °C for one hour, and then heated to 80 °C, a bubble-like texture is observed, Fig. 3c. While **2** is not observed to form nucleation crystals or fringed disc-like crystals similar to those formed by **1** upon heating, it does form disc-like crystals upon cooling from the isotropic phase, Fig. 3d.

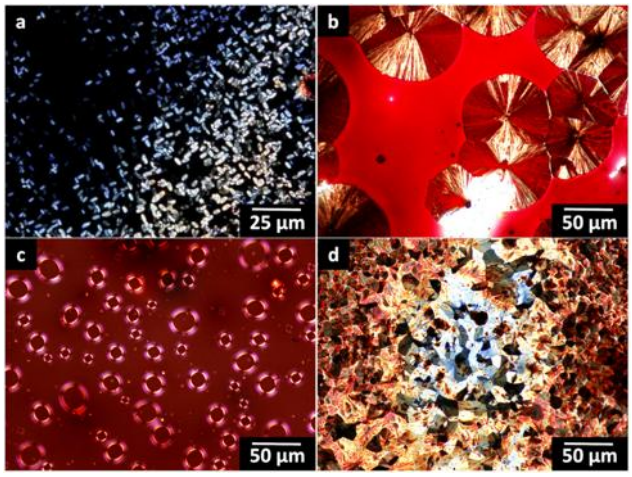

Fig. 3 HS-POM Textures: (a) **1** heated at 60 °C for 60 minutes, cross-polarized, (b) **1** heated at 90 °C for 35 minutes, (c) **2** cooled to –80 °C for 60 min and then heated to 80 °C for 60 minutes, (d) **2** heated to isotropic liquid and then cooled to 80 °C for 90 min.

For all four species, HS-POM observations revealed that crystallization can be induced by cooling from isotropic melt to a temperature within the observed DSC crystallization exotherms. The cooling exotherm associated with this

crystallization was observed in the DSC for **3** and **4**, but not for **1** and **2**. Likely, both **1** and **2** rapidly reach a temperature of reduced flexibility owing to their shorter alkyl arms. This results in amorphous frustrated solids which cannot further organize or crystallize. This is supported by the slower relative rate of crystallization upon cooling observed via HS-POM for **1** and **2** compared to **3** and **4**. Disc-like structures of **1** and **2** formed on the timescale of 30 to 90 minutes while **3** and **4** fully crystallized within 3 minutes.

All substances possess a temperature range through which they can nucleate and another range through which they can crystallize.[27] Nucleation typically occurs at lower temperatures than crystallization, but the two ranges can overlap. When the two ranges do overlap, crystallization upon cooling can occur. The crystallization observed via HS-POM upon cooling confirms that the nucleation and crystallization temperature ranges overlap for all four species.

To further investigate the kinetics of the cold crystallization, the Avrami,[28,29] Ozawa,[30] and Mo[31] methods of kinetic analysis were applied to the variable rate non-isothermal DSC data for **1** and **2**.[32] The Ozawa and Avrami models can elucidate the growth dimensionality of the crystals while the Mo model adds information about the rate of crystallization and allows for comparison of the Avrami and Ozawa models.[33]

Avrami analysis.[28,29] The fractional degree of crystallization can be expressed as

$$X(T) = \frac{\int_{T_0}^{T_C}\left(\frac{dH_C}{dT}\right)dT}{\int_{T_0}^{T_\infty}\left(\frac{dH_C}{dT}\right)dT} = \frac{\Delta H_T}{\Delta H_C} \qquad (1)$$

where ΔH_T is the enthalpy of crystallization at a given temperature and ΔH_c is the overall enthalpy of the total crystallization process.[34] T_0, T_c, and T_∞ denote temperatures at the initial crystallization event, at the desired time point, and completion, respectively. The fractional crystallinity can be converted from the temperature domain, *X(T)*, to the time domain, *X(t)*, for each non-isothermal heating rate, Fig. 4.

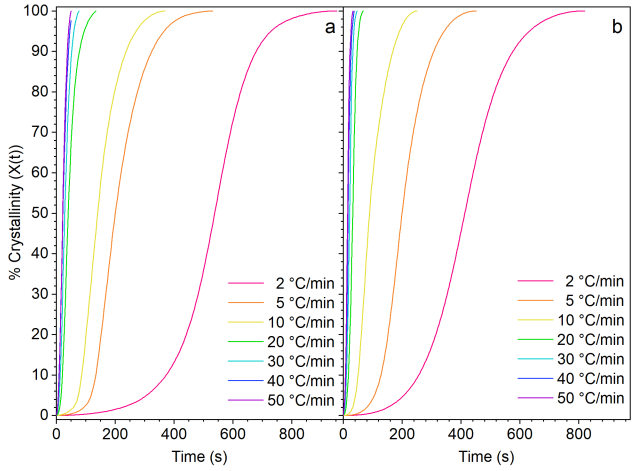

Fig. 4 Degree of crystallinity as a function of time for **1** (a) and **2** (b).

The time-domain fractional crystallinity can be fitted using the linear rearrangement of the Avrami equation.

$$\log(-\ln(1 - X(t))) = \log k + n \log t \qquad (2)$$

A plot of log(–ln(1–*X*(*t*))) vs. log(*t*), where *X*(*t*) is degree of crystallinity at time *t*, yields a linear fit for each heating rate, Fig. 5. From these linear fits, *k*, the Avrami rate constant and *n*, the crystal growth dimensionality are extracted from the intercept and slope, respectively, Table 1.

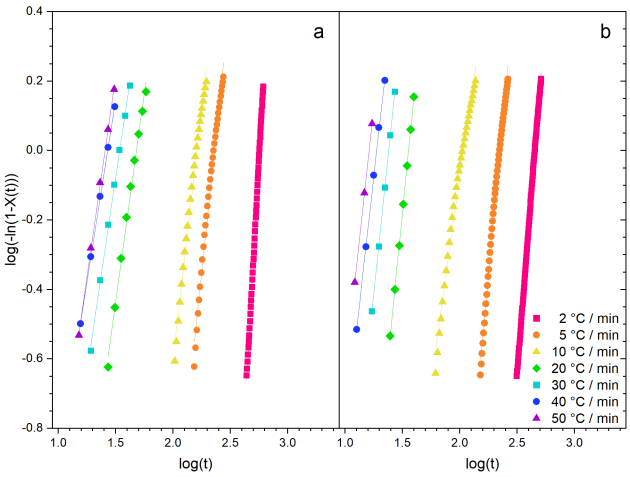

Fig. 5 Linearized Avrami plots for **1** (a) and **2** (b) cold crystallization.

Table 1 Avrami parameters for **1** and **2**.

Rate (°C/min)	*n* (1)	*k* (1)	*n* (2)	*k* (2)
2	5.84 ± 0.02	7.59×10^{-17}	4.10 ± 0.01	1.27×10^{-11}
5	3.17 ± 0.07	3.26×10^{-8}	3.52 ± 0.05	5.35×10^{-9}
10	2.89 ± 0.06	4.19×10^{-7}	2.33 ± 0.06	1.82×10^{-5}
20	2.40 ± 0.07	9.09×10^{-5}	3.34 ± 0.02	6.51×10^{-6}
30	2.23 ± 0.04	3.77×10^{-4}	3.17 ± 0.02	4.17×10^{-5}
40	2.10 ± 0.02	9.99×10^{-4}	2.95 ± 0.04	1.70×10^{-4}
50	2.31 ± 0.03	5.57×10^{-4}	3.03 ± 0.05	2.15×10^{-4}

Avrami treatment has drawbacks that can be amplified in non-isothermal conditions. If there is appreciable secondary crystallization, *n* is less accurate especially in the latter part of the curve.[30,34] This is because the crystallization rate is reduced as crystallizing fronts collide and secondary crystallization competes, rendering the values incomparable with those obtained at early stages of conversion.[35] Because secondary crystallization is slower at lower temperatures, it has a lesser impact on dynamic non-isothermal observations. Avrami analysis of the non-isothermal DSC data revealed variable Avrami exponents that included values greater than four for both species at the slowest heating rates. These values are not physically possible with regard to crystal growth dimensionality, and when variable Avrami exponents are observed, it is attributed to the combination of crystal growth and thermal nucleation occurring simultaneously.[31] For both species, slower heating rates also show significant deviations from linearity once higher degrees of crystallinity are reached, while at faster rates, the Avrami plots remained linear up to 100% crystallization. These rate-dependent deviations indicate competing crystallization and/or nucleation events and the observed Avrami *n* describes the complete set of crystallization and nucleation events occurring at a given heating rate.

For **1**, the convergence of *n* values to between 2 and 3 in the faster heating rates indicates two-dimensional growth as the primary crystallization. The significant drop in *n* as heating rate increases suggests that nucleation is slow relative to the primary crystallization at the faster heating rates. It is likely that the formation and growth of the oblong crystals observed in HS-POM are being captured in the slower heating, yielding the observed higher values for *n*.

For **2**, *n* values of around 3 suggest that there is either simple three-dimensional growth at all heating rates or that the rate of nucleation is similar to the rate of two-dimensional crystal growth regardless of heating rate. HS-POM revealed no slow nucleation crystal growth for **2** as was observed for **1** which could be consistent with either simple three-dimensional growth or a mixture of nucleation and two-dimensional growth.

The Avrami exponents, which combine crystal growth and nucleation, change with heating rates for both species.[34] We observed nucleation and crystal growth occurring at similar rates at low temperatures in the HS-POM for **1**. Therefore, it can be concluded that multiple growth and nucleation processes are occurring simultaneously for both species, but Avrami analysis cannot not fully describe this system. Further, for all heating rates, there are two separate kinetic exotherms indicating primary and secondary crystallization processes. When slow-heating-rate Avrami exponents deviate to values greater than four, a secondary crystallization process likely exists and may consist of a slow diffusion-controlled filling of gaps within the crystal and/or a reorganization crystallization step of disordered crystals, i.e., crystal perfection.[31] Regardless of the mechanism, further analysis that can account for and confirm the presence of multiple growth or nucleation steps is necessary.

Ozawa analysis.[30] While Ozawa analysis has been successfully applied to describe dynamic solidification,[35] it neglects secondary crystallization which can lead to reduced fit;[30] however, it clearly shows if different processes are occurring at varying heating rates by applying linear form of the Ozawa equation.

$$\log(-\ln(1-X(T))) = \log Z(T) + m(T)\log\psi \qquad (3)$$

A plot of log(–ln(1–*X*(*T*))) versus log ψ, where *X*(*T*) is fraction crystalized at a given temperature and ψ is the heating rate in °C /min, yields a series of linear fits for each temperature, Fig. 6. The Ozawa parameters of log *Z*(*T*), the crystallization rate parameter describing how fast non-isothermal crystallization proceeds, and *m*, crystal growth dimensionality, are obtained from the intercept and slope, respectively, Table 2.

If the same set of crystallization processes are occurring at each heating rate, each Ozawa plot will consist of a series of parallel lines.[34] For both **1** and **2**, two sets of linear ranges for dynamic heating rates are observed. Heating rates of 2 to 10 °C/min give one set of co-linear plots and 20 to 50 °C/min give a different set of co-linear plots. For both **1** and **2**, the Ozawa exponents are not constant which indicates multiple crystallization and/or nucleation processes.[32] The non-linearity of the Ozawa plots for all heating rates complements the results

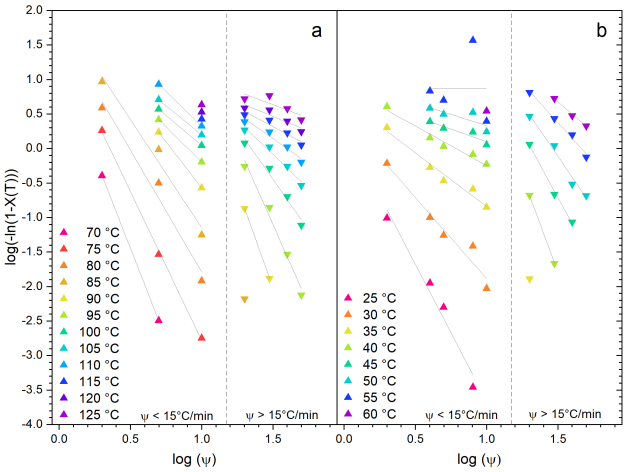

Fig. 6 Ozawa plots for **1** (a) and **2** (b).

Table 2 Ozawa parameters for **1** and **2**.

	Slow heat (ψ < 15 °C/min)			Fast heat (ψ > 15 °C/min)		
Species	***T*** **(°C)**	***m***	**log *Z*(*T*)**	***T*** **(°C)**	***m***	**log *Z*(*T*)**
1	70	5.28	1.19	90	5.78	6.65
	75	4.31	1.53	95	4.67	5.91
	80	3.54	1.75	100	2.96	3.99
	85	3.14	1.99	105	1.99	2.91
	90	2.68	2.11	110	1.46	2.34
	95	2.04	1.84	115	1.10	1.97
	100	1.76	1.80	120	0.86	1.76
	105	1.69	1.89	125	0.77	1.79
	110	2.02	2.34			
2	25	3.98	0.31	40	5.60	6.61
	30	2.35	0.47	45	3.76	4.94
	35	1.55	0.71	50	3.03	4.43
	40	1.15	0.90	55	2.29	3.80
	45	0.73	0.83	60	1.80	3.38
	50	0.65	0.98			

of the Avrami analyses, in that it also indicates multiple crystallization and nucleation events. Furthermore, it helps to identify specific rate-dependent groupings. The very high *m* values at the lowest temperatures for both species suggest that at low temperatures, both crystal growth and nucleation are occurring at similar rates.[31]

When log *Z*(*T*) changes with temperature, it indicates a variation in dominance of competing nucleation and growth processes.[31] When *m* and log *Z*(*T*) change in the same manner, as observed in fast heating for both species, crystallization rate and molecular mobility are coupled.[18] Conversely, at the slow heating rates, *m* decreases and then levels out with increasing temperature, but log *Z(T)* increases modestly, indicating that molecular mobility is not coupled with crystallization.

These data in conjunction with HS-POM observations for **1** suggest which mechanisms are competing throughout the crystallization processes. For the faster heating rates, the crystals quickly grow causing neighbouring crystals to collide or impinge. This impingement stunts further two-dimensional growth and leaves only diffusion or crystal perfection as possible growth mechanisms.[18] While it's not clear which is occurring, primary crystallization has clearly been impeded.

At slower heating rates for both species, log *Z(T)* values initially increase modestly, matching HS-POM observations that nucleation and crystal growth occur at similar rates at lower temperatures for **1**. They then stop increasing at temperatures for which two-dimensional crystal growth has been observed as the primary stage of growth with isothermal HS-POM. When **1** is heated slowly, both *m* and log *Z(T)* values cease to vary at higher temperatures. This indicates that primary crystallization dominates, as supported by HS-POM observations showing that the crystals don't reach the size at which they impinge, Fig. 3b.

Mo analysis.[31] Mo's equation is well-suited for describing non-isothermal growth kinetics in cases where multiple crystallization and/or nucleation events occur on a similar timescale.[31,33,34,36–38] The Mo equation combines and rearranges eqns (2) and (3)

$$\ln \psi = \ln F(T) - b \ln t \qquad (4)$$

where ψ is heating rate, t is the time in seconds at which a given degree of crystallinity is reached for a given heating rate, $F(T) = [K(T)/Z_t]^{1/m}$ is a kinetic parameter that decreases as the crystal growth rate increases, and b is the ratio of the Avrami and Ozawa exponents ($b = n/m$). Plotting ln ψ versus ln t for various degrees of crystallinity yields a straight line with slope $-b$ and intercept ln *F(T)* for simple crystallization. In species exhibiting competing crystallization mechanisms, there is a break in linearity between scan rates which exhibit different predominant processes. The "slow" and "fast" scan rates for both **1** and **2** show separate linear trendlines, confirming the validity of the Mo model, Fig. 7 and Table 3. These results align with the outcome of the Ozawa analysis and support the existence of competing crystallization processes.

For both **1** and **2**, the Mo plots show a change in slopes between the 10 and 20 °C/min heating rates, consistent with the Ozawa analysis. This suggests the presence of two regimes dominated by different competing crystallization and growth processes. The observed break in the linear trend for both molecules is consistent with HS-POM observations, which indicate that at slow scan rates, both nucleation and growth are initially significant, while at fast scan rates, crystal growth becomes predominant due to slower nucleation relative to the growth rate.

In most plots, the *b* values are greater than 1, or *n* is larger than *m*. Higher *b* values correlate with increased nucleation and growth rates, resulting in a larger fraction crystallized.[27] For both molecules, the *b* values are slightly higher for fast heating than for slow, except at over 80% crystallization for **1**. In all other cases for both species, *b* increases with increasing degree of crystallinity. The difference between *n* and *m* gets larger at higher degrees of crystallinity, consistent with multiple growth mechanisms.[27] The increase in *b* values at higher degrees of crystallinity can be attributed to the fact that Ozawa analysis, and thus the corresponding *m* value, neglects secondary crystallization which becomes a more significant factor at the higher degrees of crystallinity.

For **1**, the ln *F*(*T*) values appear to decrease at 80% crystallized. At the fastest scan rates, the cold crystallization exotherms overlap with the already overlapping melt endotherms and crystal perfection exotherms, Fig. 1a. As a result, an apparent increase in crystallization rate and decrease in *b* are observed, contradicting other observed trends. It is unlikely for the rate to increase as a function of reaction progress; rather, the overlapping kinetic and thermal events obfuscate the cold crystallization exotherms.

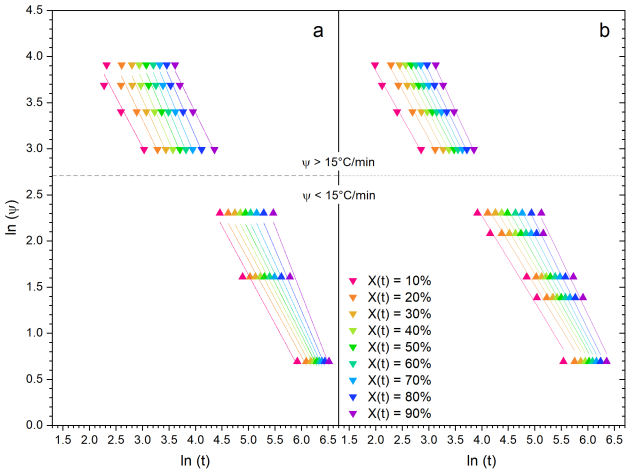

Fig. 7 Mo plots for **1** (a) and **2** (b).

Table 3 Mo parameters for **1** and **2**.

	Slow heat (ψ < 15 °C/min)			Fast heat (ψ > 15 °C/min)		
Species	***X(T)***	***b***	**ln *F(T)***	***X(T)***	***b***	**ln *F(T)***
1	10%	1.06	6.94	10%	1.09	6.28
	20%	1.05	7.02	20%	1.19	6.88
	30%	1.07	7.26	30%	1.28	7.36
	40%	1.10	7.53	40%	1.32	7.68
	50%	1.14	7.83	50%	1.34	7.95
	60%	1.19	8.17	60%	1.39	8.27
	70%	1.25	8.64	70%	1.38	8.44
	80%	1.34	9.28	80%	1.32	8.39
	90%	1.48	10.3	90%	1.18	8.11
2	10%	0.94	6.02	10%	1.02	5.89
	20%	0.95	6.24	20%	1.07	6.33
	30%	0.97	6.47	30%	1.09	6.56
	40%	1.00	6.71	40%	1.11	6.72
	50%	1.02	6.94	50%	1.11	6.85
	60%	1.07	7.30	60%	1.14	7.02
	70%	1.11	7.60	70%	1.16	7.18
	80%	1.16	8.03	80%	1.20	7.43
	90%	1.20	8.38	90%	1.26	7.84

At all heating rates for both species, the ln *F*(*T*) values, which correlate to more difficult crystallization,[38] increase with the degree of crystallinity. Crystallization rate is primarily influenced by molecular mobility and at high degrees of crystallinity, the significant portion of the material that has already crystallized restricts molecular mobility. At the highest degrees of crystallinity, the impingement of crystalline regions significantly attenuates the apparent rate of crystallization; therefore, an increase in the degree of crystallinity corresponds to a decrease in molecular mobility, leading to a decrease in the rate of crystallization.

The highest rate of crystallization is observed early in the crystallization process at faster heating rates for both **1** and **2**. The ln *F*(*T*) values increase at higher degrees of crystallinity,

indicating slower crystal growth. At any given degree of crystallinity, the ln *F*(*T*) values are greater for the slower heating rates than the faster, implying there is a slower rate of crystallization at a slower heating rate. Generally, **2** has lower ln *F*(*T*) values than **1**, indicating that **2** crystalizes more easily. This can be attributed to the longer alkyl chains on **2**, which provide greater flexibility and increased molecular mobility, thus easier crystallization.

By combining the findings from the HS-POM, Avrami, Ozawa, and Mo analyses, it is apparent that there are multiple overlapping growth and nucleation processes. For both **1** and **2**, both nucleation and two-dimensional crystal growth occur simultaneously and at similar rates at low temperatures relative to the cold crystallization exotherms. At high temperatures relative to the cold crystallization exotherms, the rate of nucleation is much slower than the rate of crystallization. While nucleation was only observed for **1** via HS-POM, the similarity of the kinetic parameters for the two species leads to the conclusion that both must behave similarly in the bulk.

Further, the variation of log *Z(T)* in the Ozawa plots indicates that the relative contributions of nucleation and growth vary with temperature. Considering the values of *m* and *Z(T)*, it becomes evident that the crystallization rate is dependent on molecular mobility only for fast heating rates. Crystal growth rate increases with increasing temperature until crystal fronts collide at high degrees of crystallinity, leading to a significant reduction in the rate of crystallization. Once crystal growth is impinged, the values of the Avrami *n* and Ozawa *m* deviate from each other as only slow diffusion filling of gaps within the crystal and crystal perfection are possible.

Conclusions

A series of four porphyrins was synthesized and found to exhibit liquid crystallinity by HS-POM and DSC. By systematically increasing the length of an alkyl spacer between two regions of relative molecular rigidity, the thermal glass and isotropic transition temperatures are decreased and the molecular mobility is increased, resulting in more facile crystallization. All four species can crystallize upon cooling from the isotropic phase.

Additionally, species **1** and **2**, which have shorter alkyl spacers, exhibited kinetic cold crystallization upon heating. The Avrami, Ozawa, and Mo methods were used to elucidate the kinetic parameters associated with the cold crystallization in bulk. These data were compared to qualitative observations obtained using HS-POM on thin films. These analyses confirmed the presence and identity of multiple overlapping growth and nucleation processes. Understanding the influence of molecular shape and flexibility on crystallization of chromophoric and birefringent small molecules facilitates the design of new functional materials.

Author contributions

Conceptualization: L.J.T., J.L.O.; Methodology: A.L.D., D.P.L., M.R.R., J.C.K., L.J.T., J.L.O.; Validation: A.L.D., C.D.M., N.Y.K., E.S., J.S.K., C.J.T., J.L.O.; Formal Analysis: A.L.D., D.P.L., C.D.M., M.R.R., C.D.M., N.Y.K., E.S., J.C.K., J.S.K., C.J.T., M.L., J.E.W., L.J.T., J.L.O.; Investigation: A.L.D., D.P.L., C.D.M., M.R.R., N.Y.K., J.C.K., J.S.K., C.J.T., M.L., J.E.W., L.J.T., J.L.O.; Resources: L.J.T., J.L.O.; Data Curation: C.D.M., N.Y.K., E.S., L.J.T., J.L.O.; Writing - Original Draft: A.L.D., D.P.L., M.R.R., L.J.T. J.L.O.; Writing - Review and Editing: L.J.T., J.L.O.; Visualization: D.P.L., C.D.M., M.R.R., N.Y.K., E.S., J.L.O.; Supervision: L.J.T., J.L.O.; Project Administration: L.J.T., J.L.O.; Funding Acquisition: L.J.T., J.L.O.

Conflicts of interest

There are no conflicts to declare.

Acknowledgements

We gratefully acknowledge funding from NSF DUE S-STEM grant 1356379 and the Multiple Investigator Cottrell College Science Award supported by the Research Corporation for Science Advancement. We also gratefully acknowledge the financial support provided by Siena college through Department of Chemistry and Biochemistry, the Stewart's Advanced Instrumentation and Technology Center, the School of Science, and the CURCA Winter and Summer Scholars Program. We would like to particularly thank Dr. K. Kolonko for guidance on thermal analyses, assistance with SEM, and many helpful discussions, Prof. R. Bachman of The University of the South for his generous loan of the Instec STC200 heated stage making HS-POM measurements possible, and our current students, especially G. Zontini, for assistance with review and editing of the manuscript.

Notes and references

1 M. Ethirajan, Y. Chen, P. Joshi and R. K. Pandey, *Chem. Soc. Rev.*, 2011, **40**, 340–362.
2 A. Yella, H.-W. Lee, H. N. Tsao, C. Yi, A. K. Chandiran, Md. K. Nazeeruddin, E. W.-G. Diau, C.-Y. Yeh, S. M. Zakeeruddin and M. Graetzel, *Science*, 2011, **334**, 629–634.
3 Y. Ding, W.-H. Zhu and Yongshu. Xie, *Chem. Rev.*, 2017, **117**, 2203–2256.
4 J. K. Sanders, N. Bampos, Z. Clyde-Watson, S. L. Darling, J. C. Hawlet, H.-J. Kim, C. C. Mak and S. J. Webb, in *The Porphryin Handbook*, eds. K. M. Kadish, K. M. Smith and R. Guilard, Academic Press, New York, 2000, vol. 3, Ch. 15, pp. 10–34.
5 H. Guo, S. Zheng, S. Chen. C. Han, F. Yang, *Soft Matter*, 2019, **15**, 8329–8337.
6 X. Zhang, Y. Xia, L. Zhou, P. Liu and W. Deng, *Tetrahedron*, 2017, **73**, 558–565.
7 B. Roy, N. De and K. C. Majumdar, *Chem. Eur. J.*, 2012, **18**, 14560–14588.
8 A. Honda, T. Yoshida, A. Shioda, K. Nomoto and K. Miyamura, *Bull. Chem. Soc. Jpn.*, 2019, **92**, 1853–1858.

9 A. Kimijima, A. Honda, K. Nomoto and K. Miyamura, *Cryst. Eng. Comm.*, 2019, **21**, 3142–3145.
10 Y. Tsujimoto, T. Sakurai, Y. Ono, S. Nagano and S. Seki, *J. Phys. Chem. B*, 2019, **123**, 8325–8332.
11 A. Concellón, M. Marcos, P. Romero, J. L. Serrano, R. Termine and A. Golemme, *Angew Chem. Int. Ed.*, 2017, **56**, 1259–1263.
12 A. Honda, Y. Takahashi, Y. Tamaki and K. Miyamura, *Chem. Lett.*, 2016, **45**, 211–213.
13 K. Ishino, H. Shingai, Y. Hikita, I. Yoshikawa, H. Houjou and K. Iwase, *ACS Omega*, 2021, **6**, 32869–32878.
14 A. A. Boopathi, S. Sampath and T. Narasimhaswamy, *New J. Chem.*, 2019, **43**, 9500–9506.
15 S. Sampath, A. A. Boopathi and A. B. Mandal, *Phys. Chem. Chem. Phys.*, 2016, **18**, 21251–21258.
16 H. Achira, I. Yoshikawa and H. Houjou, *Chem. Lett.*, 2016, **45**, 1415–1417.
17 K. Iwase, Y. Toyama, I. Yoshikawa, Y. Yamamura, K. Saito and H. Houjou, *Bull. Chem. Soc. Jpn.*, 2018, **91**, 669–677.
18 T. Rozwadowski, Y. Yamamura and K. Saito, *Cryst. Growth Des.*, 2021, **21**, 2777–2785.
19 B. Neises and W. Steglich, *Angew. Chem. Int. Ed. Engl.*, 1978, **17**, 522–524.
20 A. Sakakura, K. Kawajiri, T. Ohkubo, Y. Kosugi and K. Ishihara, *J. Am. Chem. Soc.*, 2007, **129**, 14775–14779.
21 W. R. Dichtel, S. Hecht and J. M. J. Fréchet, *Org. Lett.*, 2005, **7**, 4451–4454.
22 M. Jasiurkowska-Delaporte, T. Rozwadowski, E. Dmochowska, E. Juszyńska-Gałązka, P. Kula, and M. Massalska-Arodź, *J. Phys. Chem. B*, 2018, **122**, 10627–10636.
23 M. Jasiurkowska-Delaporte, T. Rozwadowski, E. Juszyńska-Gała Zka, J. Krawczyk, E. Dmochowska, P. Kula, and M. Massalska-Arodź, *Eur. Phys. J. E,* 2019 **42**, 121.
24 Z. Chen, J. Yu, R. Teerakapibal, L. Meerpoel, R. Richert, and L. Yu, *Soft Matter*, 2020, **16**, 2025–2030.
25 Z. Chen, C. Bishop, E. Thoms, H. Bock, M. D. Ediger, R. Richert, and L. Yu, *Chem. Mater.*, 2021, **33**, 4757–4764.
26 S. Solarski, M. Ferreira and E. Devaux, *Polymer (Guildf)*, 2005, **46**, 11187–11192.
27 T. Rozwadowski, M. Massalska-Arodź, A. Kolek, K. Grzybowska, A. Bak and K. Chedowska, *Cryst. Growth Des.*, 2015, **15**, 2891–2900.
28 M. Avrami, *J. Chem. Phys.*, 1939, **7**, 1103–1112.
29 M. Avrami, *J. Chem. Phys.*, 1940, **8**, 212–224.
30 T. Ozawa, *Polymer (Guildf)*, 1971, **12**, 150–158.
31 T. Liu, Z. Mo, S. Wang and H. Zhang, *Polym. Eng. Sci.*, 1997, **37**, 568–575.
32 J. Málek, N. Koga, L. A. Pérez-Maqueda and J. M. Criado, *J. Therm. Anal. Calorim.*, 2013, **113**, 1437–1446.
33 X. Li, M. Zou, L. Lei and L. Xi, *Polymers*, 2021, **13**, 3713–3723.
34 G. Z. Papageorgiou, D. S. Achilias, D. N. Bikiaris and G. P. Karayannidis, *Thermochim. Acta.*, 2005, **427**, 117–128.
35 M. L. di Lorenzo and C. Silvestre, *Prog. Polym. Sci.*, 1999, **24**, 917–950.
36 A. Deptuch, T. Jaworska-Gołąb, M. Marzec, M. Urbańska and M. Tykarska, *Phase Transit.*, 2019, **92**, 126–134.
37 Ł. Kolek, M. Jasiurkowska-Delaporte and E. Juszyńska-Gałązka, *J. Mol. Liq.*, 2021, **323**, 115040–115051.
38 I. Keridou, L. J. Del Valle, L. Funk, P. Turon, L. Franco and J. Puiggalí, *Molecules*, 2019, **24**, 2840–2864.